POLITECNICO
MILANO 1863

DIPARTIMENTO DI MECCANICA

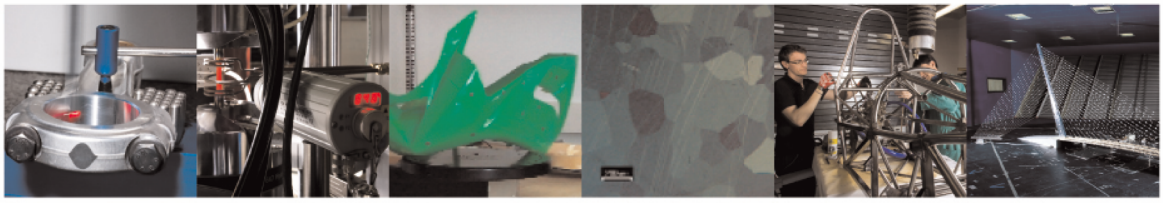

Densification behaviour of pure copper processed through cold pressing and binder jetting under different atmospheres

Romano T.;Migliori E.;Mariani M.;Lecis N.;Vedani M.

This is a post-peer-review, pre-copyedit version of the article Romano,Tobia;Migliori, Emanuele;Mariani, Marco;Lecis, Nora;Vedani, Maurizio, Rapid prototyping journal, 23 May 2022, Vol. 28, Issue 6, pages 1023 - 1039. The final authenticated version is available online at: http://dx.doi.org/RPJ-09-2021-0243

Densification behaviour of pure copper processed through cold pressing and binder jetting under different atmospheres

Abstract

Purpose – Binder jetting is a promising route to produce complex copper components for electronic/thermal applications. This paper aims to lay a framework for determining the effects of sintering parameters on the final microstructure of copper parts fabricated through binder jetting.

Design/methodology/approach – The knowledge gained from well-established powder metallurgy processes was leveraged to study the densification behaviour of a fine high-purity copper powder (D_{50} of 3.4 μm) processed via binder jetting, by performing dilatometry and microstructural characterization. The effects of sintering parameters on densification of samples obtained with a commercial water-based binder were also explored.

Findings – Sintering started at lower temperature in cold-pressed (~680 °C) than in binder jetted parts (~900 °C), because the strain energy introduced by powder compression reduces the sintering activation energy. Vacuum sintering promoted pore closure, resulting in greater and more uniform densification than sintering in argon, as argon pressure stabilizes the residual porosity. About 6.9% residual porosity was obtained with air sintering in the presence of graphite, promoting solid-state diffusion by copper oxide reduction.

Originality/value – This paper reports the first systematic characterization of the thermal events occurring during solid-state sintering of high-purity copper under different atmospheres. The results can be used to optimize the sintering parameters for the manufacturing of complex copper components through binder jetting.

Keywords Binder jetting, Additive manufacturing, Powder metallurgy, Copper, Dilatometry, Sintering

Paper type Research paper

1. Introduction

Additive manufacturing (AM) of high-purity copper is attracting the attention of academic and industrial researchers owing to great potential advantages in the manufacturing of devices with complex shape and possibilities of integration of functions. With its superior electrical and thermal properties, the use of copper is of particular interest in the sectors of electronic devices and thermal management systems (Tran *et al.*, 2019). As compared to conventional fabrication methods, such as metal casting, welding, and machining, the layer-by-layer approach of AM offers an utmost design freedom that can be exploited to produce complex welding inductors, electric motor components (Ledford *et al.*, 2020), and heat exchangers to enable a new generation of power generators for portable electronic devices (Bai and Williams, 2015).

However, some of the intrinsic properties of copper lead to significant processing challenges for laser and electron beam powder bed fusion (L-PBF and EB-PBF, respectively) AM technologies. The high thermal conductivity of copper rapidly conducts heat away from the melt area, resulting in high local thermal gradients and solidification rates (El-Wardany *et al.*, 2018). These aspects result in high residual stresses, that can lead to part distortion and solidification cracking. Additionally, the low amount of localized heat may result in poor interlayer adhesion, leading to part delamination (Colopi *et al.*, 2018a). (Lykov, Baytimerov, *et al.*, 2016) demonstrated that preheating the building substrate at 140 °C can reduce the porosity in pure copper parts manufactured via LPBF by avoiding rapid heat loss from the melt area. However, adopting this solution requires the use of a more complex machine setup (Jiang *et al.*, 2021). Infrared radiation from above was successfully employed by (Chen *et al.*, 2020) to reduce heat dissipation during selective laser sintering (SLS) of a high-performance polymer. However, this approach cannot be easily extended to pure copper because the energy absorption provided by infrared radiation on copper is very limited (Gruber *et al.*, 2021). Due to copper's high reflectivity, most of the energy provided by the laser in L-PBF is reflected instead of being absorbed by the powder. This results in residual porosity in the final parts due to incomplete fusion of the powder when employing a conventional 200 W infrared fibre laser, leading to relative densities of less than 90% (Lykov, Safonov, *et al.*, 2016; Silbernagel *et al.*, 2019; Trevisan *et al.*, 2017). Previous studies (Colopi *et al.*, 2018b; Ikeshoji *et al.*, 2018; Jadhav *et al.*, 2021) showed that increasing the laser power above 500 W can lead to relative densities higher than 96%. However, high-power lasers can generate unstable melt tracks due to the different absorptivity of the powder and the molten material, resulting in poor surface finish of as-built parts (Gruber *et al.*, 2021). In addition, the large amount of reflected energy that irradiates the optical mirror of the machine during the printing process may damage it when a high-power infrared laser is employed

(Jadhav *et al.*, 2019). Although (Gruber *et al.*, 2021) demonstrated the use of a green laser source to manufacture pure copper parts with relative densities higher than 99.8%, most commercial machines for LPBF are equipped with infrared lasers (Trevisan *et al.*, 2017). Another challenge faced when processing copper by PBF is that the low viscosity of molten copper makes it difficult to control the melt pool, which tends to spread across the melting path/surface. Therefore, powder feed rate and build platform movement along the build (Z) direction need to be coordinated to adjust melt viscosity and, thus, the thickness of the deposit (Onuike *et al.*, 2018). (Lodes *et al.*, 2015) reported that pure copper powders tend to stick to the melt surface during raking due to the high tendency to sintering of copper, thus generating pores and binding defects in the deposits and hindering post-building powder removal and recycling. Finally, special care in handling and storage of powder feedstocks is required due to copper's high sensitivity to oxidation (El-Wardany *et al.*, 2018; Ledford *et al.*, 2019; Tran *et al.*, 2019), as pre-existing oxides in the powder cannot be easily removed during the printing process and can lead to crack formation in the as-built parts (Guschlbauer *et al.*, 2020).

Binder jetting is an emerging AM technology that allows overcoming the above limitations of DED and PBF technologies for the processing of high-purity copper. The binder jetting process consists of a series of independent steps, as depicted in Fig. 1:

a) Printing of the part geometry layer by layer through selective deposition of a liquid polymeric binder onto the powder bed to join the powder particles according to the 3-dimensional model fed to the printer.
b) Curing of the powder bed at mild temperature (roughly at about 200 °C) to promote binder polymerisation, thus improving the green part strength for easy handling, and to extract the green parts from the unbound powder (de-powdering process).
c) Debinding treatment at around 450 °C to remove the residual polymer (brown part formation).
d) Sintering at high temperature to ideally achieve full density in the final parts.

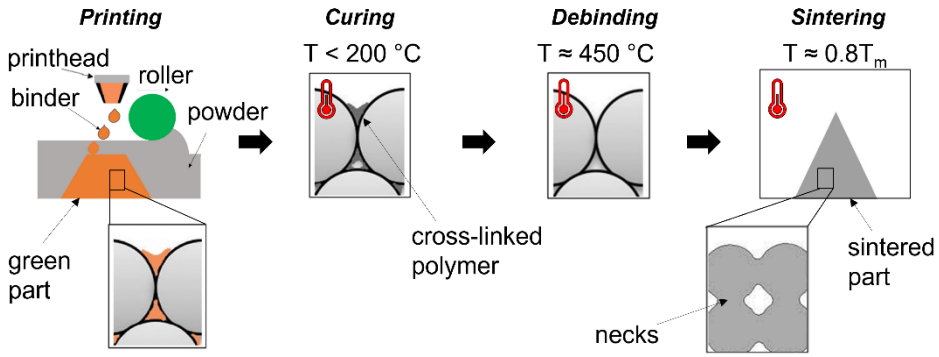

Fig. 1 – Schematic representation of binder jetting process. Adapted from (Bai and Williams, 2015, 2018a).

Binder jetting presents some advantages over DED and PBF technologies for the processes of high-purity copper because it functionally separates part creation from particle sintering, thus circumventing the challenges associated with melting and solidification of copper powders. Specifically, it avoids issues related to residual stress build-up due to rapid melting and solidification of the powder and does not require the design and use of support structures for heat dissipation and part anchoring purposes, because the powder bed acts as an inherent support for overhanging features (Kumar *et al.*, 2017; Yegyan Kumar *et al.*, 2018). Since no laser beam is involved in the printing process, binder jetting shows no concern for the high optical reflectivity of copper (Tran *et al.*, 2019). Also, oxides that may be present in the powder feedstock can be conveniently removed during the sintering process by employing a proper reducing atmosphere. The independence of printing and sintering steps also makes binder jetting inherently scalable by simply increasing the size or number of printer nozzles or printheads (Yegyan Kumar *et al.*, 2018), as it does not require an enclosed chamber and expensive energy sources (Bai and Williams, 2015). In addition, several parts can be built in a single job by stacking them in the powder bed, as the excess loose powder can be easily removed in the post-processing stage, resulting in increased productivity, and collected for recycling.

The primary challenge in binder jetting is to achieve full density after sintering, because green parts are made of loosely packed particles with low inherent sinterability, as the roller cannot effectively compact the powder particles during layer recoating. This reduces the availability of neck-forming sites (Kumar *et al.*, 2017) and possibly leads to residual porosity in the final parts, which is a major defect for applications that require high thermal and electrical conductivity.

The use of binder jetting for the manufacturing of highly pure copper was firstly explored by (Bai and Williams, 2015) but limited research has been conducted so far.

(Bai and Williams, 2018b) used a colloidal organic binder enhanced with suspended copper nanoparticles and an inorganic copper nanosuspension ink to print pure copper parts via binder jetting. They found that, while the jetted nanoparticles produced denser green parts, there was no significant difference in density after sintering compared to parts printed with a conventional organic binder. (Bai and Williams, 2018a) used a metal-organic-decomposition (MOD) ink as a precursor for copper nanoparticle precipitation during sintering. Sintered parts had a denser core section than parts printed with a conventional polymeric binder. However, a porous outer shell with large pores formed around the dense core, because the use of the MOD ink resulted in insufficient green part strength after curing, which caused loss of powder from the surface of printed parts during the de-powdering operation. Further studies by the same group (Bai *et al.*, 2017; Yegyan Kumar *et al.*, 2019) reported the benefits of bimodal powder mixtures in binder jetting of pure copper parts, improving powder flowability, green and sintered part density, and reducing shrinkage upon sintering. However, a relative density of no more than 90.5% was achieved after sintering at 1075 °C. (Miyanaji *et al.*, 2020) investigated binder jetting of fine copper powder with average particle size of 5 μm, employing standard water- and solvent-based binders. A maximum density of 91.2% was achieved employing the solvent-based binder and a low heating rate of 1 °C min^{-1} for reaching the sintering temperature, which was required to ensure binder removal and deoxidation before closure of the small pores in parts printed with fine powder. Samples printed with the aqueous binder showed a lower density, due to formation of water vapor hindering densification during sintering.

The goal of this work is to lay a framework of further information for determining the relationship between sintering parameters and final microstructure of high-purity copper parts fabricated through binder jetting. The knowledge gained from well-studied powder metallurgy (PM) processes was taken as a basis for the investigation, because these techniques are close in nature as they both functionally separate the part geometry creation from the sintering step. A fine high-purity copper powder, having 3.4 μm average particle size, was selected as feedstock material following the suggestions given by (Miyanaji *et al.*, 2020), who showed that the use of fine copper powders can improve the final density and properties of parts fabricated through binder jetting. This powder was processed via either cold pressing or binder jetting and its sintering behaviour was then characterized through dilatometry analyses completed with microstructural observation by means of optical and scanning electron microscopy (SEM). The results obtained with these two manufacturing routes were compared to determine the effects of powder compaction and of the polymeric binder on sinterability of highly pure copper powders. Finally, binder jetted parts were densified varying the sintering atmosphere, heating rate, peak temperature, and isothermal holding time to explore the effects of processing parameters on final part characteristics.

2. Materials and methods

2.1 Copper powder characterisation

The material used in this study was a gas atomized pure copper powder (m4p™ pureCu.04, item 70594), provided by m4p Material Solutions GmbH. The chemical composition of the powder provided by the manufacturer is listed in Table I.

Table I

Particle shape and size distribution of the as-received powder were characterized by static image analysis (Morphologi 4, MalvernPanalytical) with 20x and 50x lens (the analysed range of particle size was 0.150 μm - 130 μm and >1.6E10^6 particles were analysed) on a dry powder dispersed sample. Particle geometry, chemical composition, and crystal structure of the powder were analysed using a Zeiss Sigma 500 field-emission scanning electron microscope (FE-SEM) with energy dispersive spectroscopy (EDS) X-ray detector and a Rigaku SmartLab X-ray diffractometer at a scanning rate of 1° min^{-1} in the range of 20–100° (step 0.020°; Cu-Kα radiation λ = 1.5406 Å) at 40 kV and 40 mA with Bragg-Brentano geometry. Powder apparent density and tap density were measured with a FT4 Powder Rheometer® to evaluate powder packing efficiencies. The ratio of apparent density to tap density (Hausner ratio, HR) was used to assess powder flowability, considering that a lower HR ratio corresponds to better flowability (Li *et al.*, 2020):

$$HR = \frac{\rho_t}{\rho_{ap}} \quad (1)$$

Three powder samples were heated in air at 180 °C for 2, 4, and 6 hours, respectively, in a Yamato DX412C drying oven to evaluate the effects of air curing on material purity. A Zeiss EVO 50 SEM microscope was used to qualitatively evaluate the extent of oxidation in cured powder samples by performing EDS microanalysis. X-ray diffraction (XRD) was conducted to determine which oxidized phases formed during air curing.

2.2 Specimen manufacturing processes

Cold-pressed samples were fabricated using a universal testing frame (MTS Exceed E45 model equipped with 100 kN load cell), employing a steel die with a rectangular cavity of 5 x 30 mm^2. In each compaction experiment, an amount of about 7 g of copper powder was poured in the die and compacted up to a final load of 50 kN, corresponding to a compaction stress of about 333 MPa, with 1 mm min^{-1} punch displacement rate at room temperature. The tools were not lubricated to avoid contamination of copper samples. In Fig. 2, the measured axial load is plotted versus the punch displacement. A good reproducibility in the four pressing tests performed was observed.

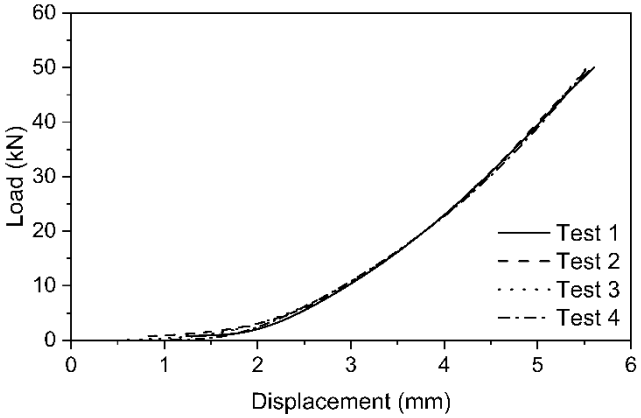

Fig. 2 – Load-displacement curves recorded during the cold compaction tests.

30 x 5 x 5 mm^3 binder jetted bars were printed with an ExOne Innovent+® printer, employing a standard aqueous polymeric binder (AquaFuse) provided by ExOne, and the printing parameters listed in Table II. An in-house designed reduced build volume device was adopted to reduce the bed width and printing volume (Fig. 3(a)), in order to avoid using large amounts of copper powder for small-volume prints and to shorten the printing times.

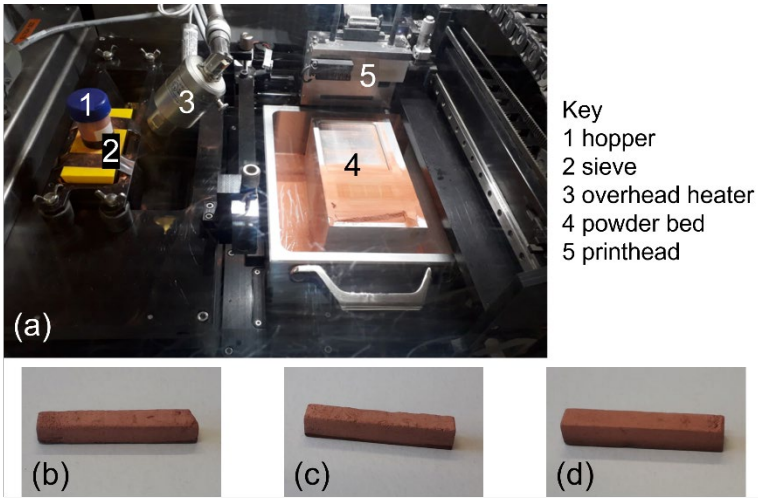

Fig. 3 – Views of (a) ExOne Innovent+® printer and powder bed during the binder jetting process and samples printed with (b) 90, (c) 100, and (d) 110 BS ratio after curing.

In the ExOne BJ system, the feedstock powder contained in the hopper passes through a sieve to break particle agglomerates before being deposited on the bed. Sieving and spreading of the powder is assisted by ultrasonic vibrations induced by transducers. 75% ultrasonic intensity (UI) was used following the suggestions given by (Miyanaji *et al.*, 2020), who showed that increasing the UI in the range 25-75% improves the density of green

parts fabricated with fine copper powders. All the specimens were aligned on XY plane so that the thickness of the samples was along the build direction (Z). Only samples printed along the XY direction were considered in this investigation which was mainly focussed on densification behaviour and related microstructure of parts manufactured through binder jetting. The use of a fine powder allowed for the selection of a small layer thickness of 50 μm. Although reducing the layer thickness increases the duration of the printing process, the use of thin layers improves the surface finish of printed parts by reducing staircase effects and enhances the inter-layer bonding (i.e., green strength) by facilitating binder penetration into a powder layer (Miyanaji *et al.*, 2020). From Table II it can be noticed that the binder saturation (BS) ratio was varied from 90% to 110% to evaluate its effect on final part density. The BS ratio is the percentage of the air space between powder particles that is occupied by the binder (Bai and Williams, 2015). It must be high enough to allow for sufficient binder penetration between layers, but not so high that binder penetrates wider regions of the powder bed than intended (Kumar *et al.*, 2017), leading to distortion even of the green parts. Fifteen samples were printed for each value of the BS ratio and then cured in air at 180 °C for 6 hours to polymerize the binder and improve green part strength for easy de-powdering and handling (Fig. 3(b-d)).

Table II

Following printing and curing, some binder jetted samples were sintered in an industrial furnace with atmosphere control provided by FILMS S.p.A. – OMCD Group. The sintering cycle (Fig. 4(a)) featured a reducing hydrogen/nitrogen atmosphere with 50% hydrogen to promote copper oxide reduction during sintering. A 60-min isothermal hold at 450 °C was applied to burn-off the binder. After the debinding step, the temperature was increased to 900 °C, where it was held for 3 hours. Heating ramps at a rate of 1 °C min^{-1} were used between the holding stages.

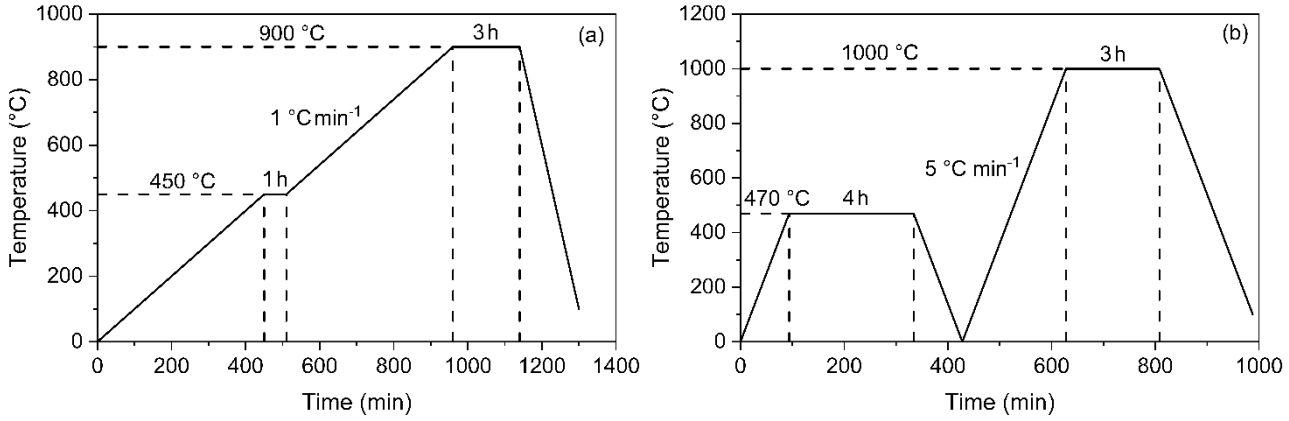

Fig. 4 – (a) Sintering cycle applied in an industrial furnace and (b) debinding and sintering cycle applied in a muffle furnace.

Other specimens printed with a fixed BS ratio of 90% were subjected to a debinding treatment at 470 °C for 4 hours in argon atmosphere with 5 °C min^{-1} heating rate. After debinding, four brown (debinded) specimens were sintered in a muffle furnace with atmosphere control, applying a heating rate of 5 °C min^{-1} and 3-hour isothermal holding at 1000 °C (Fig. 4(b)). The first sample was sintered under inert argon atmosphere. The second sample was sintered in argon in presence of graphite to create a reducing atmosphere containing carbon monoxide (CO) aimed at reducing the copper oxide according to the equations (Jones and Taylor, 1923; Liu *et al.*, 1999):

$$2CuO + CO \rightarrow Cu_2O + CO_2 \quad (2a)$$

$$Cu_2O + CO \rightarrow 2Cu + CO_2 \quad (2b)$$

The third sample was placed inside a graphite crucible and covered with a further plate of graphite to have the entire sample surface in contact with graphite to improve the oxide reduction. Finally, the fourth sample was placed inside a graphite crucible and sintered in air environment.

2.3 Green and debinded part characterisation

The density of as-pressed parts was determined by the immersion method based on Archimedes' buoyancy principle, using a Mettler Toledo scale and employing ethanol as liquid for volume determination. The density was calculated using the equation:

$$\rho = \frac{w_{air} \cdot \rho_{eth}}{w_{air} - w_{eth}}$$

(3)

where w_{air} is the mass of the sample in air, w_{eth} is the apparent mass of the sample when it is immersed in ethanol, and ρ_{eth} is the density of ethanol at 22 °C (0.7875 g cm^{-3} (Khasanshin and Aleksandrov, 1984)). The density of the printed samples was then calculated by the measured weight and dimensions of the parts. A Nikon Eclipse LV250NL optical microscope and a Zeiss Sigma 500 were used to observe the morphology of green parts. The values reported here are average of at least five measurements.

The thermal behaviour of the debinded parts was characterised through differential scanning calorimetry (DSC) and thermogravimetric (TG) analysis, using a SETARAM LABSYS calorimeter, to determine phase transformations and oxidation/reduction reactions that may occur during sintering of the investigated samples. Both analyses were performed in inert argon atmosphere by increasing the temperature at a heating rate of 20 °C min^{-1}, from 20 to 1100 °C, reaching the liquid stage of copper (the melting point of copper is 1085 °C (Bernard *et al.*, 2005)).

2.4 Dilatometry analysis

A Linseis L75 vertical dilatometer was used to study the dilatometric behaviour of cold-pressed (CP) and green (G) and brown (B) binder jetted samples, to predict the onset temperatures of the thermal events occurring during sintering and to evaluate the effects of compaction and of the polymeric binder on the sinterability of the copper powders. Dilatometry experiments were performed in argon atmosphere (1.2 bar argon pressure; 2 nl h^{-1} flow rate) and under medium vacuum (10^{-2} mbar), as reported in Table III. Experimental parameters such as the heating rate, peak temperature, and isothermal holding times were varied for the different samples according to the plot given in Fig. 5.

Table III

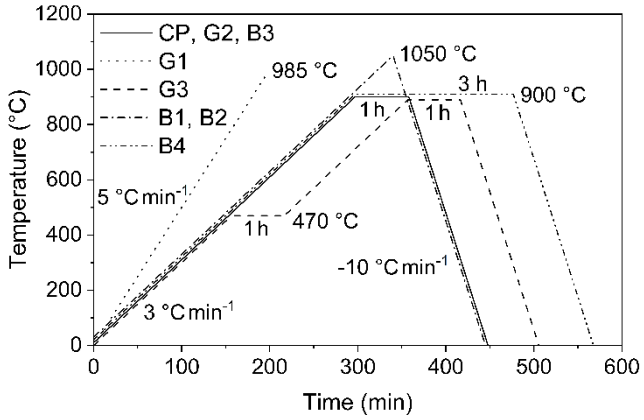

Fig. 5 – Thermal profiles used in the dilatometry experiments.

Once the heating steps were completed, the samples were cooled down to room temperature with a 10 °C min^{-1} cooling rate. This fast cooling prevented any significant amount of sintering from occurring during the ramp-down phase, allowing the shrinkage measurements on cooling to be used for calculating the coefficient of thermal expansion (CTE) (Wheat *et al.*, 2020). The CTE value is required to correct the dilatometry data to represent only shrinkage due to sintering, eliminating the contribution of the thermal expansion/shrinkage of the copper particles, which individually behave as a pore-free volume when they are subjected to a thermal cycle. The trend of the linear CTE as a function of temperature was determined from the dilatometric curves using the formula:

$$\alpha = \frac{1}{L_1}\frac{\Delta L_2 - \Delta L_1}{T_2 - T_1} = \frac{1}{L_0 + \Delta L_1}\frac{\Delta L_2 - \Delta L_1}{T_2 - T_1}$$

(4)

$\Delta L_2 - \Delta L_1$ is the change of sample length due to temperature variation from T_1 to T_2. Since the cooling ramp was not applied to sample G1, its CTE was calculated from the linear portion of the dilatometric curve, from about 50 °C to 190 °C, where no event is likely to occur except the material thermal expansion itself (Johnston *et al.*, 2004).

2.5 Sintered sample characterisation

Both the sintered samples produced by binder jetting and those consolidated during the dilatometry analyses were grinded and polished following standard metallographic procedures (600, 1200, 2500 grit abrasive papers and 6 and 1 µm diamond pastes). Their microstructure was characterized through optical and SEM microscopy, completed with image analysis with ImageJ software to measure the residual porosity of sectioned and etched surfaces. EDS was performed to qualitatively evaluate the impurity content in sintered parts. The cold-pressed sample was chemically etched immersing its surface for 5 s in a solution of 10 g ferric chloride, 50 ml hydrochloric acid, 10 ml nitric acid and 100 ml water to reveal its microstructure through selective chemical attack of grain boundaries.

The Vickers microhardness of the samples consolidated during dilatometry and sintered in the muffle furnace was determined with a Future-Tech FM-700 microhardness tester. 50 g load and 15 s dwell time were used in the tests. The reported values are the averages of at least five measurements taken from the areas that showed a more extensive densification on the polished cross-section of each sample. The samples sintered in hydrogen atmosphere were not tested as they did not undergo any significant densification during the sintering process.

3. Results and discussion

3.1 Powder characterisation

The feedstock powder consisted of mostly spherical particles (mean circularity value of 0.93) with size distribution ranging from about 0.5 µm to 11 µm and 3.4 µm average particle size, as shown in Fig. 6. This is among the smallest powder reported in literature regarding powder-based AM processes. It was selected on the basis of the study by (Miyanaji *et al.*, 2020) on the effects of fine powders on the quality of pure copper parts fabricated via binder jetting. In Table IV data about tap and apparent density as well as Hausner ratio are provided. In binder jetting, particles larger than 20 µm in diameter are usually preferred (Bai and Williams, 2015) to facilitate spreading and recoating with the counter-rotating rolling system. Indeed, it is reported that finer powders often exhibit poor sliding and tend to agglomerate, due to interparticle friction caused by the large van der Waals cohesive forces established among small particles with large surface area (Mariani *et al.*, 2021). However, in the present investigation, the Hausner ratio of 1.14, which is below the threshold of 1.2 considered as the upper acceptable limit for free-flowing powders, indicates that the copper powder has a good flowability despite its small size possibly due to its almost spherical shape (see Fig. 6(c-d)).

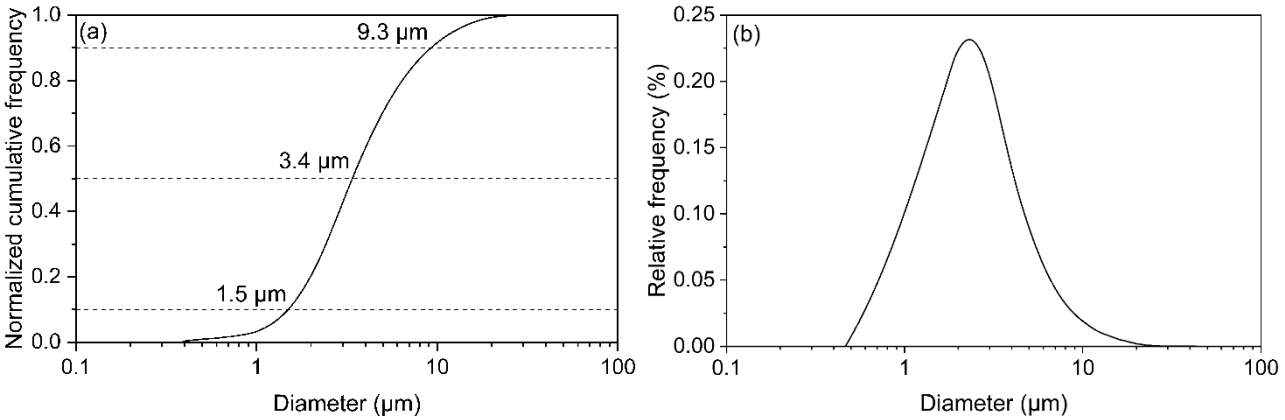

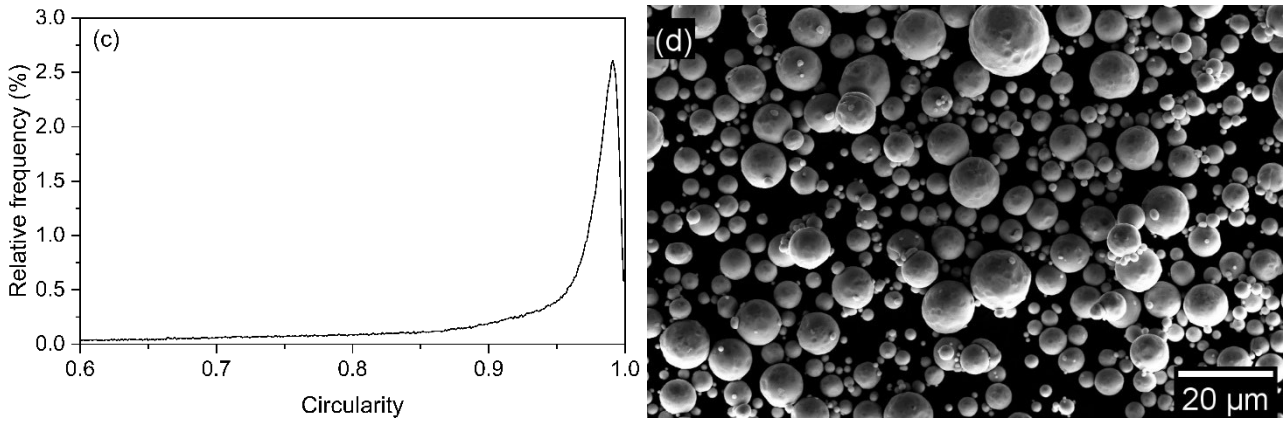

Fig. 6 – Cumulative distribution (a), relative distribution (b), circularity (c), and SEM micrograph (d) of the as-received powder.

Table IV

Fig. 7 shows the XRD patterns of the copper powder in the as-received state and after curing at 180 °C for 2, 4, and 6 hours, in the 2ϑ interval 35-40°. A weak peak can be observed at 38.9° in the pattern of the as-received powder and its intensity remains nearly unchanged with increasing the curing time. This diffraction peak can be attributed to the (111) reflection plane of the CuO monoclinic phase. (Choudhary *et al.*, 2018) showed that the thermal oxidation of copper in air only produces CuO above 320 °C, when the value of Gibb's free energy change (ΔG) for CuO formation becomes negative. This suggests that this phase presumably formed during the gas atomization process rather than during air curing. The intensity of the peak at 36.5°, corresponding to cuprous oxide Cu_2O (111) reflection, slightly increases with time. According to well-established thermodynamic data, oxidation of copper powder by the water present in the aqueous binder is thermodynamically impossible (Eriksen *et al.*, 1989). However, in aerated water and under low-temperature heating, the dissolved oxygen can induce the formation of a Cu_2O layer on the surface of copper particles according to the equation (Eriksen *et al.*, 1989):

$$2Cu + \frac{1}{2}O_2 \rightarrow Cu_2O$$

(5)

Indeed, above 150 °C, oxygen molecules can diffuse through the thin native oxide layer spontaneously formed on copper surface producing further oxidation, as the thermal energy helps to overcome the diffusion barrier (Choudhary *et al.*, 2018). The intensity of the oxygen peaks observed in the EDS patterns of cured powder samples did not significantly increase by increasing the curing time from 2 to 6 hours. Therefore, it was possible to extend the curing time to 6 hours to improve the strength of green parts still avoiding extensive oxidation of the copper powder.

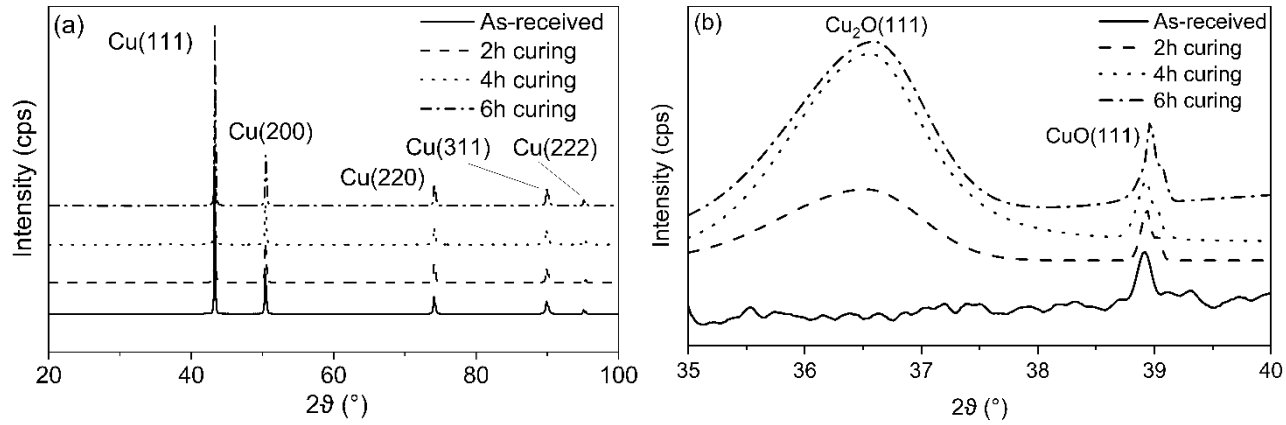

Fig. 7 – XRD patterns in the 2ϑ intervals (a) 20-100° and (b) 35-40° of copper powder as-received and cured at 180 °C for 2, 4, and 6 hours.

3.2 Green part characterisation

The densities of the green parts fabricated by cold pressing and by binder jetting are reported in Table V. As compared to results available in the literature (Castrejón-Sánchez *et al.*, 2019; Olmos *et al.*, 2014; Raship *et al.*, 2017), a considerably high as-pressed density was obtained with a relatively low compaction pressure of about 333 MPa. This can be attributed to the high fraction of very fine particles smaller than 2 µm in diameter, which are supposed to be able to fill the gaps between the larger ones, resulting in a high density due to a tighter particle packing. The SEM picture of an as-pressed sample (Fig. 8(a)) shows that copper particles are well packed and have been plastically deformed under the applied compression load, losing their initial spherical shape.

Table V

Considering the data given in Table V, it can be stated that the density of the binder jetted samples increases by increasing the BS ratio, as a larger faction of space volume between powder particles is occupied by the binder. These values are comparable to those reported by (Miyanaji *et al.*, 2020) for similar powder characteristics and printing parameters. The small standard deviation recorded suggests a good reproducibility of the printing process, confirming that the powder has suitable flow properties for binder jetting, despite its small size. Finally, the layered structure of a binder jetted sample can be observed in Fig. 8(b). Compared to the sample CP, the powder particles in the binder jetted part are loosely packed (see inset in Fig. 8(b)) and retained their spherical shape, as no significant pressure is applied during the printing process.

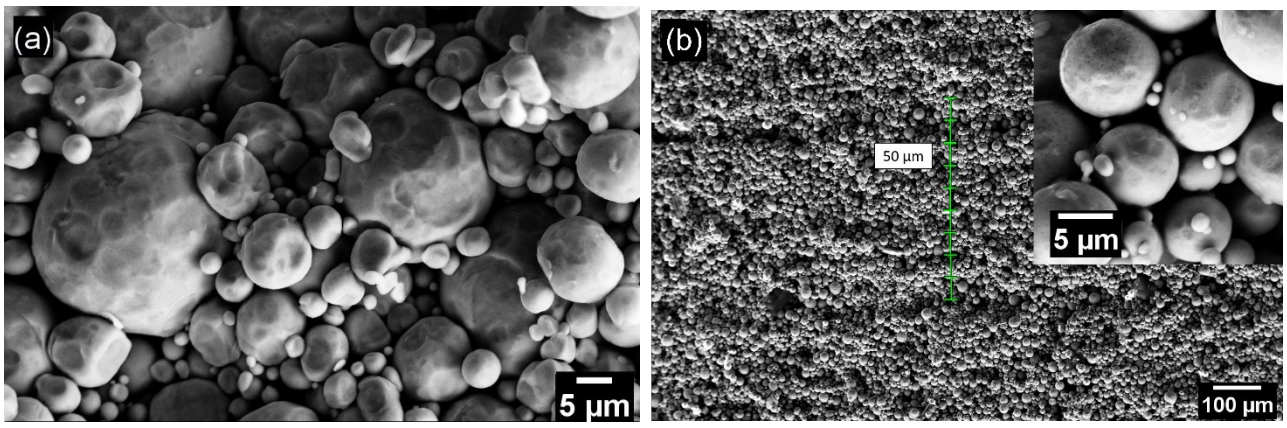

Fig. 8 – SEM micrograph of (a) as-pressed and (b) binder jetted (BS110) samples. The green ruler highlights the layered structure of the binder jetted sample.

3.3 Debinded part characterisation

Fig. 9 shows the DSC and TG plots of a representative debinded sample in the temperature interval 0-1000 °C. The exothermic DSC peak centred around 450 °C can be attributed to reduction of CuO to Cu_2O starting around 300 °C with the involvement of residual carbon produced by the binder pyrolysis (Li *et al.*, 1991):

$$4CuO + C \rightarrow 2Cu_2O + C + O_2$$

(6a)

$$C + O_2 \rightarrow CO_2$$

(6b)

The two exothermic peaks above 600 °C can be attributed to reduction of Cu_2O to Cu involving carbon residues (Liu *et al.*, 1999):

$$2Cu_2O + C \rightarrow 4Cu + CO_2$$

(7)

The exothermic DSC peak around 900 °C can be attributed to sintering of copper particles, which indicates that necking and densification begin to occur around this temperature, while a strong endothermic peak at around 1085 °C (not shown in this graph) corresponds to melting of the material.

The sudden drop in the TG curve at about 140 °C can be attributed to the removal of moisture (Sabzevari *et al.*, 2016) and other contaminants that remained in the porous sample after the debinding operation. The progressive mass loss starting from around 300 °C is due removal of oxygen when copper oxides are reduced according to Eq. (6a) and (7).

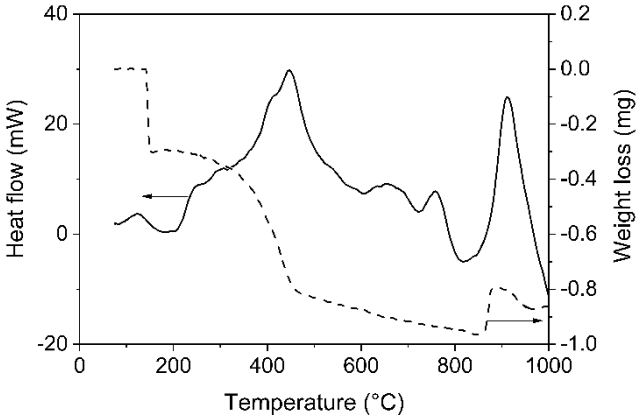

Fig. 9 – DSC and TG plots of a representative debinded sample in the temperature interval 0-1000 °C.

3.4 Dilatometry

Table VI depicts the mean CTE values obtained for cold-pressed and binder jetted samples. The variability in the CTE values of the binder jetted parts is attributed to the different degree of densification achieved in the samples after sintering.

Table VI

Fig. 10(a) shows the dilatometric curve of the sample CP. After correction with the estimated mean CTE, the whole curve becomes negative, indicating that the first increasing part is due to thermal expansion of the individual copper particles before relevant densification occurs at higher temperatures. It can be observed that the cooldown portion of the curves becomes approximately flat, indicating that the estimated CTE value is appropriately correcting for the thermal shrinkage. The onset temperatures of thermal events observed in the dilatometric plots were graphically estimated with the Onset toolbar in OriginPro software. Five measurements were taken varying the amplitude of the considered interval. The values reported hereafter in the text are the averages of these estimates. The sintering onset temperature of sample CP is about 680.8 °C. This agrees with previous studies (Champion *et al.*, 2003; Dominguez *et al.*, 1998; Papillon, Missiaen, *et al.*, 2017; Papillon, Roure, *et al.*, 2017) indicating that sintering of micron-size copper powders begins at half the melting point of the metal and significant shrinkage is observed around 600 °C, when volume diffusion is activated. The investigated cold-pressed sample experienced a total linear shrinkage of about 5.3%. Previous studies (Olmos *et al.*, 2014; Papillon, Missiaen, *et al.*, 2017; Papillon, Roure, *et al.*, 2017) also reported that high-density pure copper powder compacts are subjected to swelling during sintering due to gases generated by thermal decomposition of volatile products at high temperature since the produced gases cannot be evacuated due to pore closure that occurs earlier on the surface of the samples. In the present work, undesired swelling and de-densification were prevented by employing a pure copper powder with no antioxidants/lubricants, thus avoiding the generation of gaseous product decomposition during the experiment and reaching a final relative density of about 96.5%.

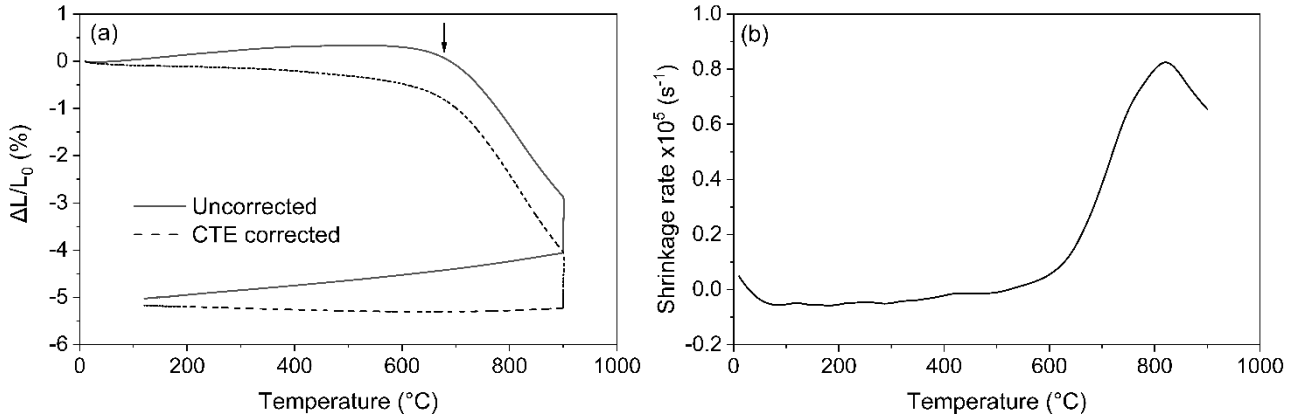

Fig. 10 – (a) Dilatometric curve and (b) shrinkage rate as a function of temperature in sample CP.

Fig. 10(b) shows the shrinkage rate dependence on temperature for the cold-pressed specimen. The plot was obtained calculating the variation of the uncorrected strain in each time interval during the heating ramp, using the equation:

$$-\frac{d(\Delta L/L_0)}{dt} = -\frac{\Delta L_2/L_0 - \Delta L_1/L_0}{t_2 - t_1}$$

(8)

The negative sign was included into the equation to obtain positive values for the shrinkage rate. The uncorrected strain was considered for the calculation because the shrinkage rate is the length variation with respect to the time, whereas the CTE is calculated from the length variation with respect to the temperature. The maximum shrinkage rate is 0.84 s^{-1} at a peak temperature of about 830 °C. A peak at approximately the same temperature has also been observed by (Dominguez *et al.*, 1998), who showed that almost all the grain growth of micrometric copper powder compacts occurs near that peak temperature. Therefore, the high shrinkage rate observed above 800 °C may be attributed to densification occurring by grain growth in this temperature range. At higher temperatures, the shrinkage rate decreases because densification slows down after the formation of isolated spherical pores at the beginning of the final stage of sintering (Balluffi *et al.*, 2005). The beginning of a plateau-like trend can be observed in the dilatometric plot just above 800 °C. This sintering end temperature is lower than that reported by (Papillon, Missiaen, *et al.*, 2017) and (Papillon, Roure, *et al.*, 2017) for powder compacts with comparable green density. It could be attributed to the lower particle size of the powder used in this work, resulting in a higher sintering driving force due to the larger surface area.

In the microstructure of the cold-pressed sample after the sintering cycle performed in the dilatometer, individual copper particles can no longer be recognized (Fig. 11). The structure consists of equiaxed grains, fairly homogeneous in size, with the presence of twins (marked by the red arrows in the inset of the figure) which indicates that recrystallization took place during the sintering process, promoted by the high temperature and the plastic deformation introduced during the powder compaction stage. Spherical residual pores located at grain boundaries confirms that the material entered the final stage of sintering, as suggested by the final decreasing trend in the plot of the shrinkage rate.

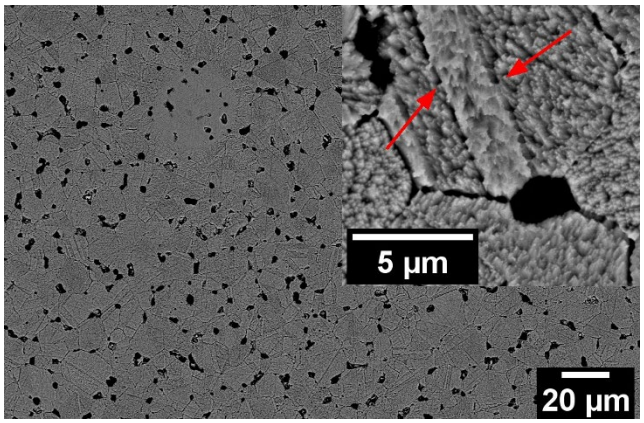

Fig. 11 – SEM micrograph of the sample CP after the sintering cycle performed in the dilatometer. The red arrows indicate the twins formed by recrystallization during sintering.

Fig. 12 shows the dilatometric curves of green binder jetted samples (G1, G2, G3). The onset temperature of the thermal events experienced by these samples during the dilatometry experiments are listed in Table VII. The first three peaks can be attributed to particle rearrangement during binder burn-out, that occurs in the temperature interval 200-450 °C. The sharp drop in curve G3 at 470 °C is due to the isothermal hold applied during the experiment. Peak n. 4 at around 600 °C can be attributed to the reduction of copper oxides (Eq. (7)), having a higher molar volume than metallic copper. Thermal event n. 5 at about 925 °C observed in curve G1 is presumably due to particle sintering occurring above 900 °C, as also displayed by DSC plots. However, this step is not very pronounced in the plot because the sample did not experience significant sintering during the experiment, as confirmed by the very limited shrinkage (compare the vertical drop at 900°C with that shown in Fig. 10(a)). It should be noted that the calculated onset temperature values are indicative only, as they were estimated with a graphical method. This also explains the high uncertainties reported.

Table VII

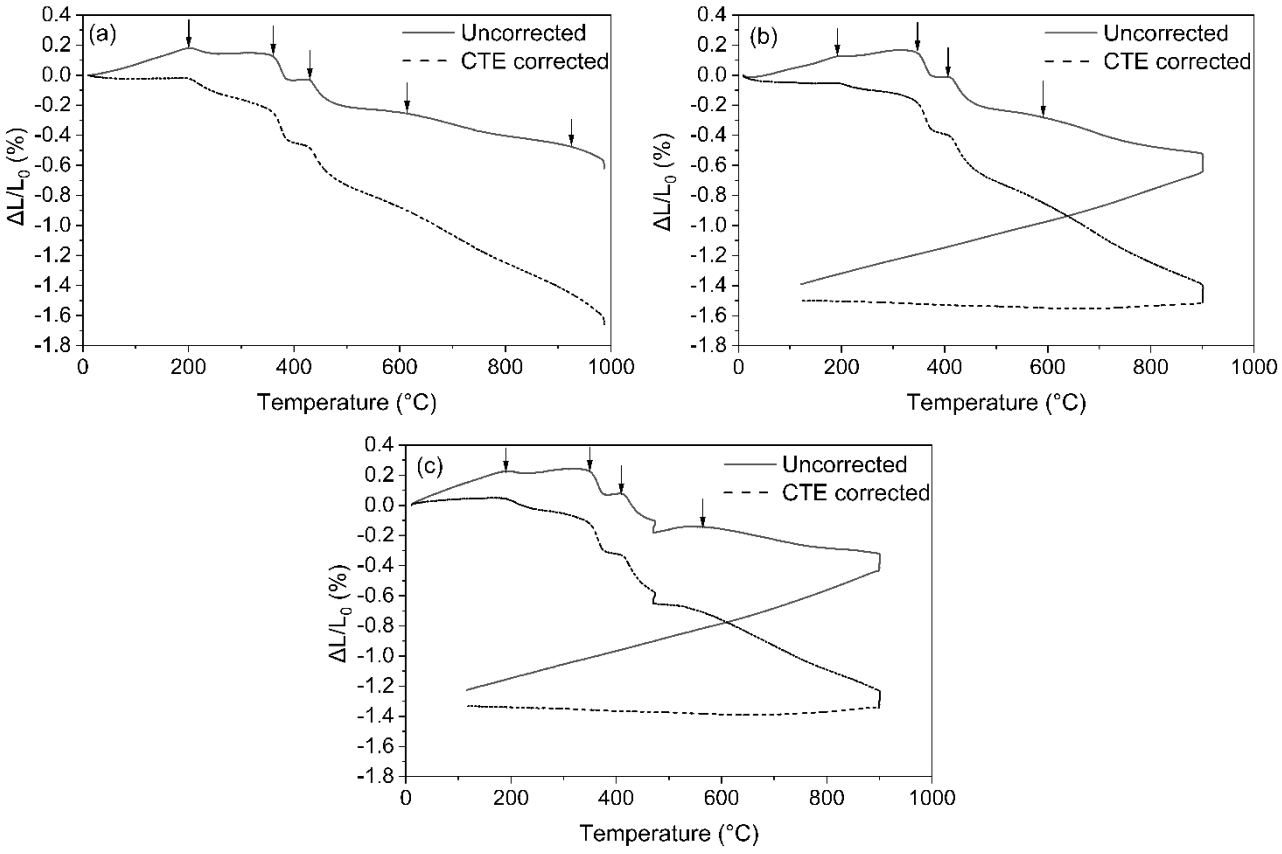

Fig. 12 – Dilatometric curves of samples (a) G1, (b) G2, and (c) G3.

The absence of significant sintering in the green binder jetted samples is also confirmed by the SEM image given in Fig. 13, recalling that they were subjected to a thermal cycle similar to that applied to sample CP. This lack of sintering is attributed to the insufficient energy provided during the applied treatment. In a powder compact, particles are brought into intimate contact and are plastically deformed. The stored strain energy is available as the driving force for sintering (Masuda, 1962) and lowers the sintering activation energy, that is the energy barrier a powder material system must overcome to start the sintering process. On the other hand, binder jetted parts are made of loosely packed particles because of the very limited pressure applied by the recoating roller during the printing process which is insufficient to significantly compact the powder and to create contact-necks between particles. This results in a lower sinterability and mass transport in the solid-state condition (Bai and Williams, 2015). Therefore, a more energy-intensive treatment (i.e., higher sintering peak temperature and longer isothermal hold) is required to induce effective sintering. Films of residual polymer can be observed in the micrograph of sample G1 (indicated by the red arrows Fig. 13(a)), that was not subjected to an isothermal holding at intermediate temperature. The 60-min hold at 470 °C applied to sample G3 removed all the residual polymer from the surface of copper particles. However, very thin flakes sticked on particle surface could still be observed in Fig. 13(b), also indicated by red arrows. These flakes are supposed to be ash residues generated by incomplete combustion of the hydrocarbon molecules generated by binder pyrolysis in non-oxidizing atmosphere (Blais, 2010), according to the equation:

$$C_nH_{m(gas)} \xrightarrow{\Delta} nC_{(soot)} + \frac{m}{2}H_{2(g)} \quad (9)$$

The process of partial combustion makes the soot slightly sticky (Blais, 2010), preventing its removal from the particle agglomerates during the debinding stage. This effect was further amplified by the use of a very fine powder, since smaller particles are more likely to absorb carbon due to their larger surface area. Therefore, it can be assumed that the lack of sintering can be also attributed to contamination produced by the soot on the surface of copper particles, hindering solid-state diffusion and neck development. No significant oxygen was detected by EDS in samples after dilatometry, confirming that reduction of copper oxides occurs even in inert argon atmosphere, presumably due to a combination of two factors:

Reaction with residual carbon produced by binder pyrolysis, as discussed in Section 3.3;

Hydrogen generated by binder decomposition (Eq. (9)), according to the reactions (Mahmoud *et al.*, 2015):

$$Cu_2O + H_2 \rightarrow 2Cu + H_2O \quad (10a)$$

$$CuO + H_2 \rightarrow Cu + H_2O \quad (10b)$$

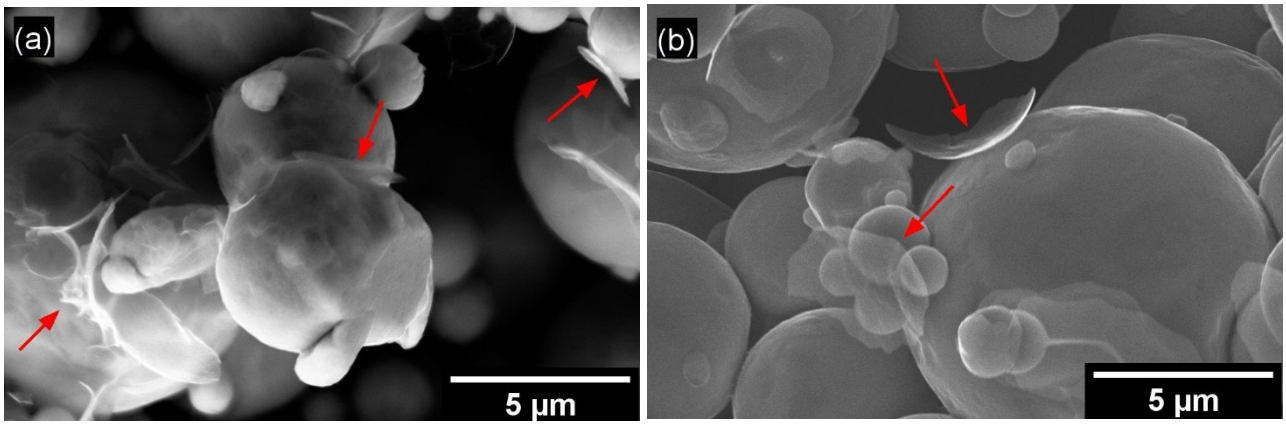

Fig. 13 – SEM views of samples (a) G1 and (b) G3 after the dilatometry tests. The red arrows indicate the polymer and ash residues observed on the surface of copper particles.

Fig. 14 shows the dilatometric curves of the brown samples (B1 tested in argon, B2, B3, and B4 tested in vacuum). The onset temperatures of the identified thermal events are listed in Table VIII. The first event at around 350 °C is due to particle rearrangement when the residual binder is burned-off. This step is less pronounced than in dilatometric curves of green samples because most of the binder was already removed during the debinding treatment. The broad peak above 600 °C is supposed to be due to copper oxide reduction, as also observed for green samples. Sintering onset occurs above 900 °C in sample B1 which was sintered in argon, as observed for green parts sintered using the same atmosphere. Parts sintered in vacuum exhibit a slightly lower sintering onset temperature. A careful observation of the curves also reveals that sample B2 experienced a much larger shrinkage than the corresponding sample B1 sintered in argon and the beginning of a plateau-like trend can be observed in the dilatometric plot above 1000 °C. These results suggest that vacuum promotes sintering densification mainly by allowing pore degassing, as also reported by (Juan, 2017) for 316L parts fabricated by binder jetting. On the other hand, in an argon atmosphere, porosity is stabilized by pressurization, which apparently hinders the densification by preventing pore closure. Finally, it must be noticed that sample B4 experienced a larger shrinkage than sample B3 because it was subjected to a longer isothermal hold at the sintering peak temperature.

Table VIII

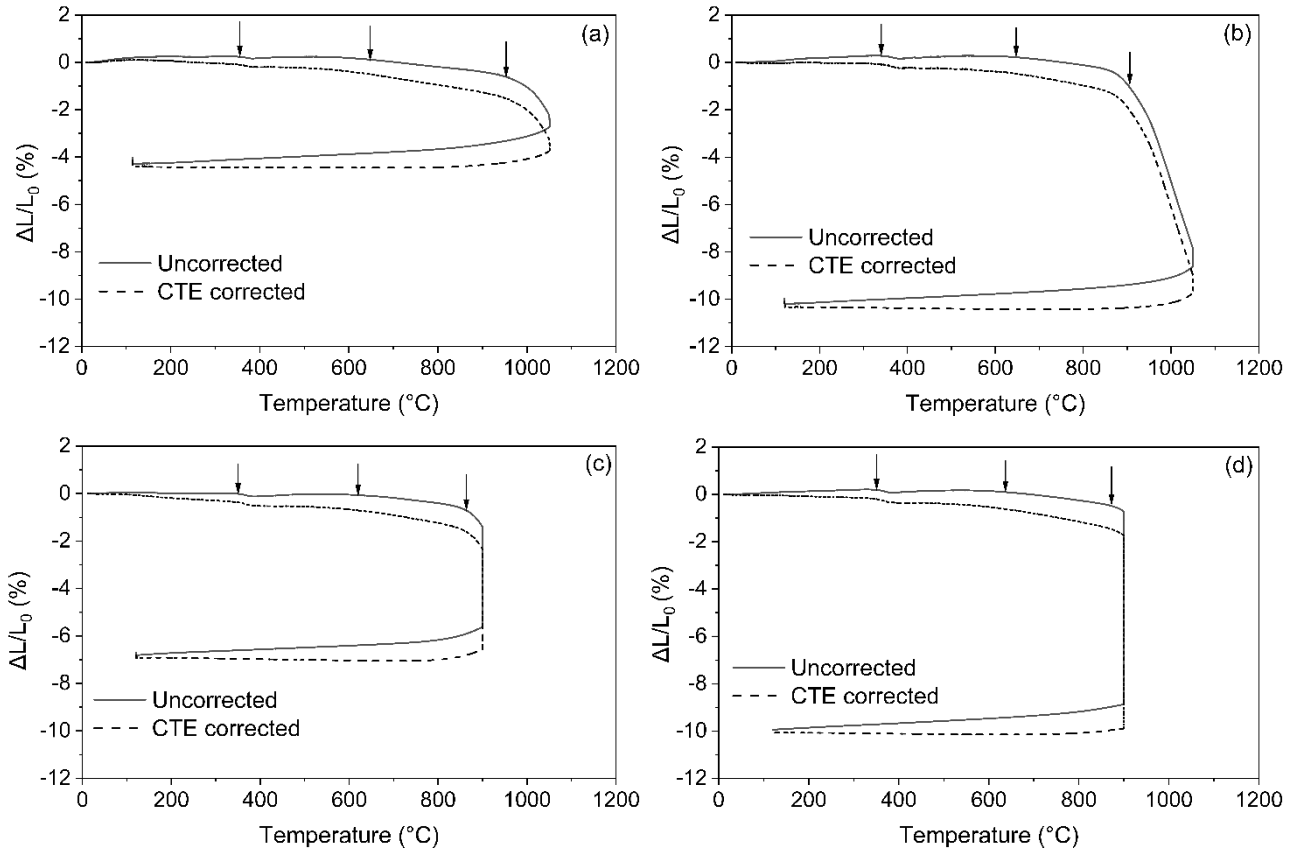

Fig. 14 – Dilatometric curves of samples (a) B1, (b) B2, (c) B3, and (d) B4.

Fig. 15 compares the shrinkage rates of samples B1 and B2, obtained applying Eq. (8) to measured data. The vacuum-sintered sample B2 experienced a maximum shrinkage rate about twice that of sample B1 (sintered in argon), which confirms that the applied negative pressure promotes pore closure by pore degassing. On the other hand, a maximum peak in the curve B1 could not be observed within the temperature range tested, indicating that higher peak temperatures would have been required to achieve pore closure when sintering under argon atmosphere. It can be noticed that the sample B2 manufactured through binder jetting showed a shrinkage rate peak at a higher temperature (about 1000 °C) than the cold-pressed sample. This is a further evidence that binder jetted parts made starting from loosely packed particles have a lower sinterability than powder compacts, and a more energy intensive sintering process is required to achieve a significant densification in the former case.

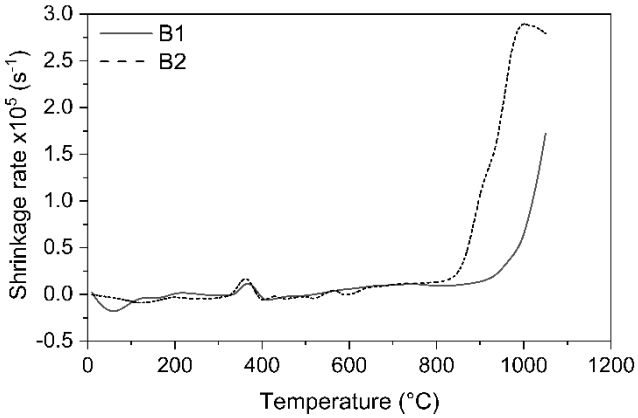

Fig. 15 – Shrinkage rate as a function of temperature for the samples B1 and B2.

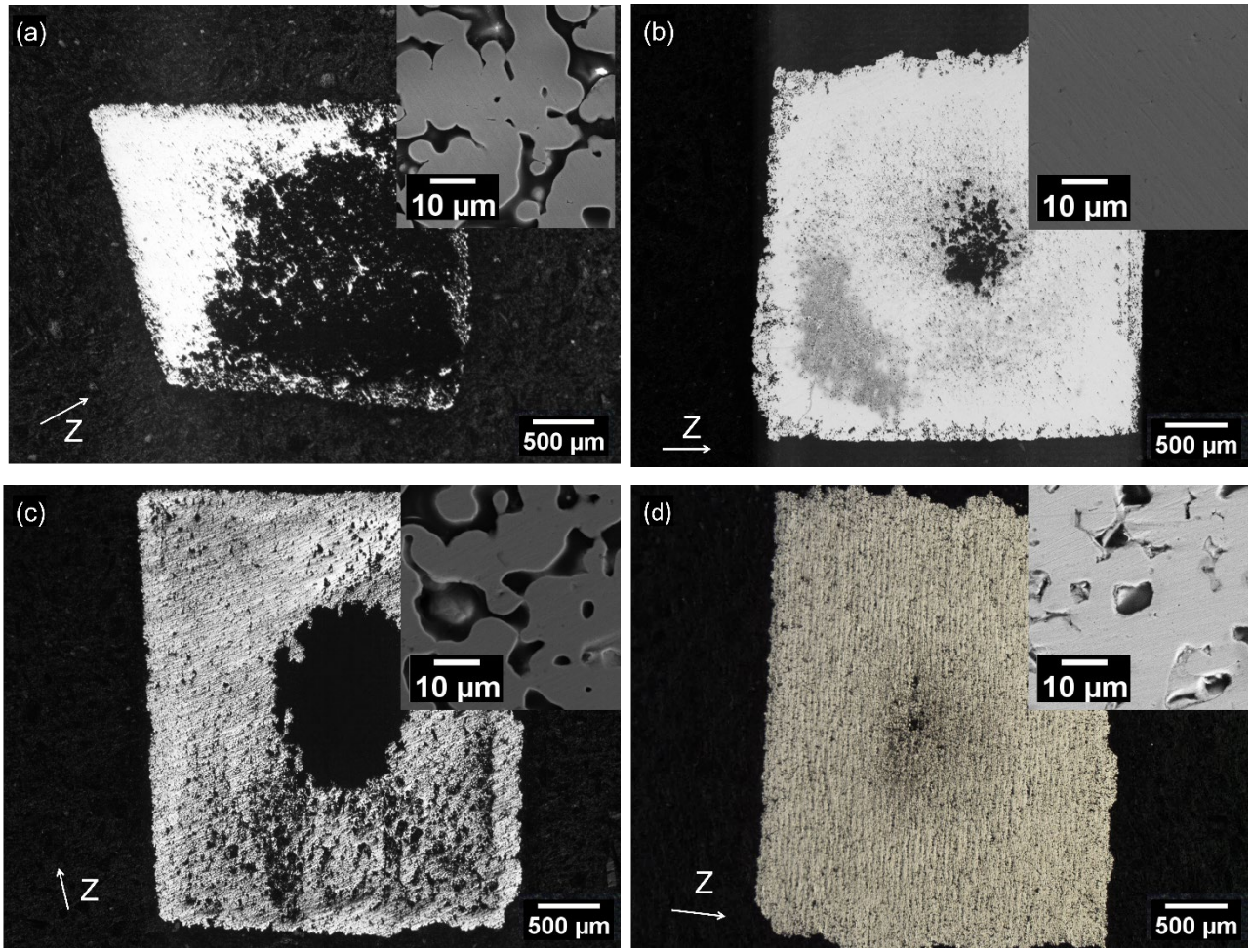

Fig. 16 – Optical and SEM micrographs of samples (a) B1, (b) B2, (c) B3, and (d) B4 after the dilatometry tests.

In Fig. 16 a collection of representative sections of the samples B1 to B4 after the dilatometry tests is depicted. Sample B1 did not homogeneously sinter during the test, as shown in Fig. 16(a). Individual particles can still be recognized in some regions, even though necks are forming among them. This inhomogeneous sintering can be attributed to the argon pressure, that promoted pore coalescence in the region that sintered last. A residual unsintered zone can be observed in the core region of sample B2 (Fig. 16(b)), as a result of the faster sintering of the outer skin (shown in the SEM picture at higher magnification) which isolated the central volume, hindering further mass transportation. However, a more uniform densification occurred as compared to sample B1 sintered in argon with the same thermal cycle, confirming that the applied negative pressure

improves the densification process. The size of the unsintered core region decreases with increasing the time-at-temperature from sample B3 to B4 (Fig. 16(c,d)). However, the outer skin of samples sintered at 900 °C (B3 and B4) shows a higher fraction of residual porosity as compared to sample B2 sintered at 1050 °C. This is an indication that a sintering temperature higher than 900 °C is required to achieve a good densification even in vacuum sintering. Overall, brown samples showed better sinterability than green parts. Therefore, the lack of sintering in green parts can be partly attributed to binder residues laying on the surface of copper particles, hindering mass transportation and necking between them.

3.5 Density and microstructure of sintered samples

The densification behaviour of binder jetted parts sintered in the industrial furnace with hydrogen-containing atmosphere is summarized in Table IX. It can be observed that these samples did not significantly densify, as confirmed by the small increase in density and the small shrinkage values. After sintering, the samples were still made of almost loose powder particles and residual polymer could be observed in the SEM micrographs of Fig. 17, indicated by the red arrows. The lack of sintering can be attributed to the insufficient energy provided to the sintering cycle and by binder contamination effects, hindering the formation of necks between copper particles, as already discussed for the green samples used in dilatometry.

Table IX

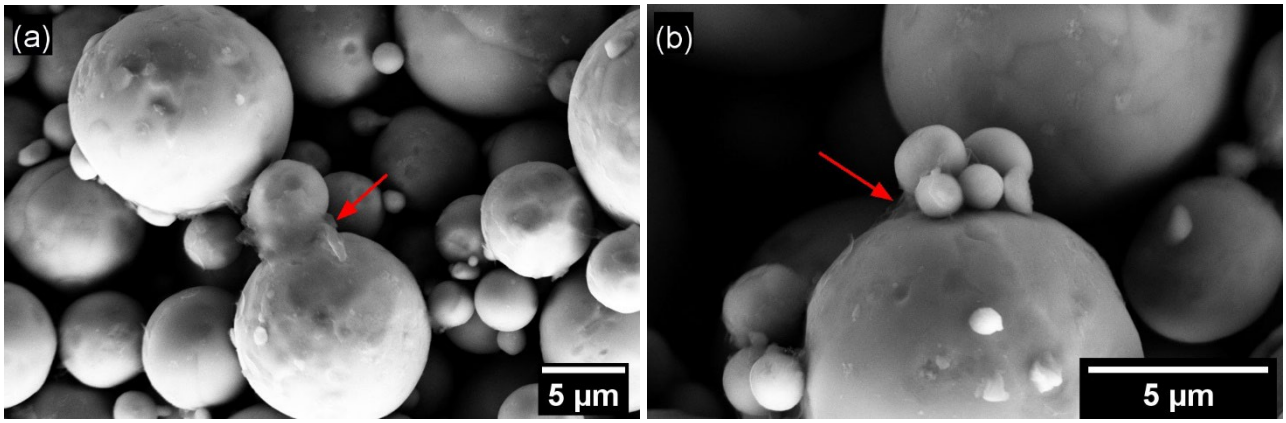

Fig. 17 – SEM micrographs of binder jetted sample (BS90) sintered in hydrogen environment. The red arrows indicate the residual polymer observed among copper particles.

Fig. 18 shows the optical and SEM micrographs of the samples sintered in the muffle furnace. An oxide shell of about 500 µm in thickness formed on the outer surface of sample A1 sintered in argon (Fig. 18(a)), possibly due to residual oxygen found in the environment of the furnace. A thinner oxide shell (about 300 µm) could be observed in sample A2 (Fig. 18(b)), as oxide formation was hindered by the presence of reducing CO in the sintering atmosphere. In addition, a lower residual porosity could be observed in the inner region of this sample, suggesting that the reducing atmosphere promoted densification. Samples A3 and A4 (Fig. 18(c-d)) were sintered inside a graphite crucible, which fully prevented the formation of an external oxide shell as the whole sample surface was in contact with graphite. Smaller and less numerous residual pores could be observed in sample A4 sintered in air as compared to samples sintered in argon atmosphere in the presence of graphite. Image analysis revealed about 19.6% and 6.9% residual porosity in samples A3 and A4, respectively. The lower porosity observed in sample A4 sintered in air can be attributed to the more efficient formation of CO in an atmosphere richer in oxygen, promoting solid-state diffusion by copper oxide reduction. It can be observed that the residual porosity in all the sintered samples is aligned perpendicular to the building direction. This residual interlayer porosity is a typical feature of parts manufactured by binder jetting (Bai *et al.*, 2017; Bai and Williams, 2018a; Kumar *et al.*, 2017; Mariani *et al.*, 2021; Yegyan Kumar *et al.*, 2018, 2019) and is attributed to the large space separating adjacent powder layers in green parts, as no significant powder compaction is provided during the printing process. Only copper peaks were observed in the EDS patterns measured in the well-sintered regions of these samples, while carbon peaks appeared when analysing the residual pores. These residual carbon impurities (estimated to exceed 8 wt% by EDS in all parts) were generated during binder burn-off and concentrated within the residual pores in the sintered parts.

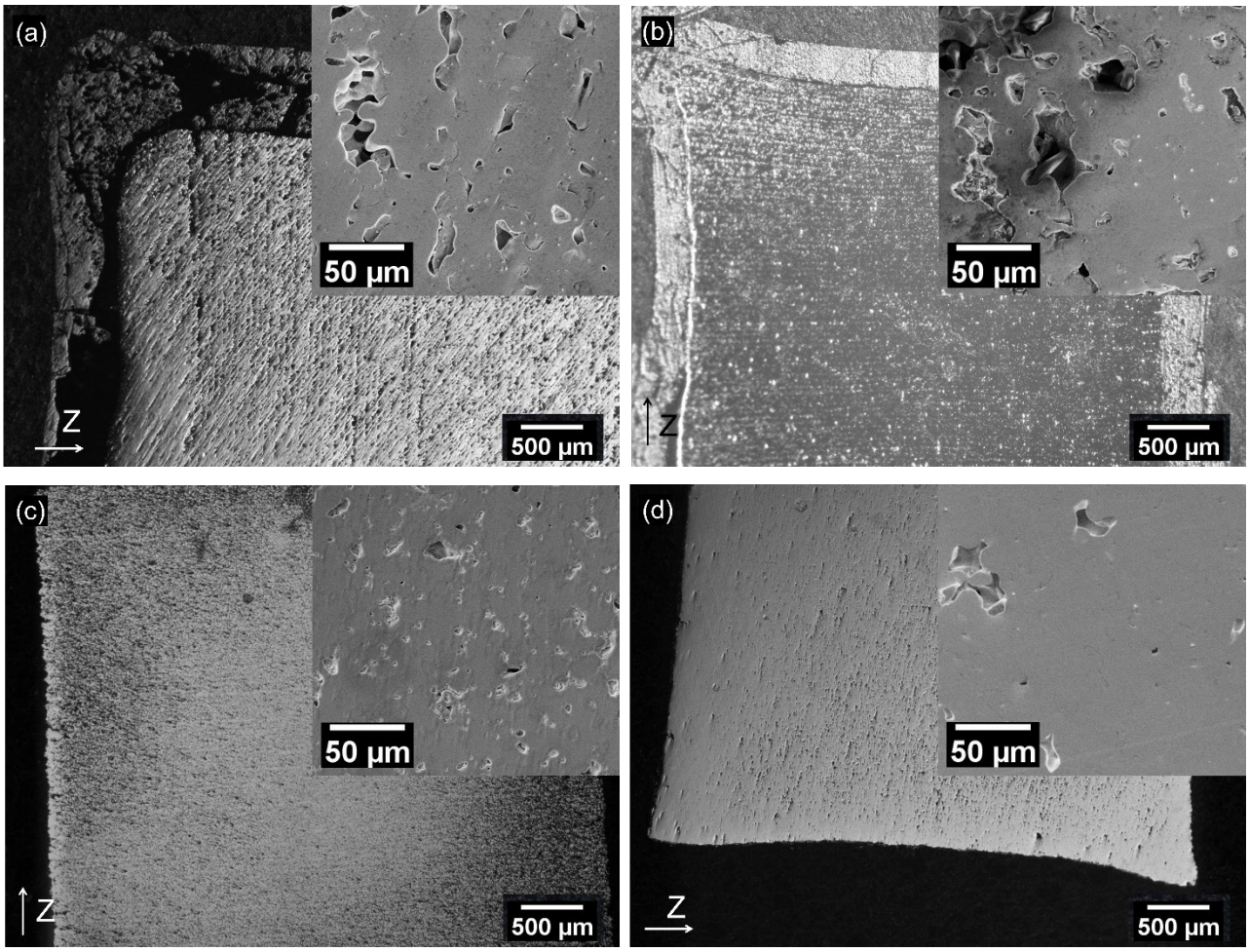

Fig. 18 – Optical and SEM micrographs of sintered samples (a) A1, (b) A2, (c) A3, and (d) A4.

3.6 Microhardness

The microhardness of the samples consolidated during the dilatometry tests and in the muffle furnace is shown in Fig. 19. Sample CP shows a much higher hardness (71.2 ± 4.3 $HV_{0.05}$) than binder jetted samples, that can be attributed primarily to the larger extent of densification experienced by this sample. Among the binder jetted samples, sample B1 sintered in argon shows the lowest hardness (20.4 ± 6.4 $HV_{0.05}$), as it experienced a very limited densification despite the high sintering temperature. Sample B2 sintered in vacuum applying the same thermal cycle has a significantly higher hardness (31.0 ± 2.3 $HV_{0.05}$), which can be attributed to the more extensive and uniform densification promoted by the negative pressure applied in the experiment. The hardness increases with increasing the isothermal holding time at 900 °C from sample B3 (27.3 ± 8.1 $HV_{0.05}$) to B4 (28.8 ± 3.4 $HV_{0.05}$). The larger dispersion observed in the measures collected on sample B3 can be attributed to the less uniform densification experienced by this sample. As regards the samples sintered in the presence of graphite, the microhardness increases with increasing the efficiency of copper oxide reduction from sample A2 to A4, that is, it follows the same trend observed in reduction of residual porosity, as discussed in Section 3.5. It can be noted that sample CP exhibits a much higher hardness than sample A4 (33.2 ± 3.4 $HV_{0.05}$), although similar levels of residual porosity were observed in these parts. This difference can be attributed to the fine microstructure generated in sample CP by recrystallization (see Section 3.4), resulting in increased hardness due to the Hall-Petch effect (Hammad, 1990). Surprisingly, sample A1 sintered in argon shows a relatively high microhardness of 31.0 ± 8.2 $HV_{0.05}$, which can be attributed to the presence of copper oxides formed in non-reducing atmosphere and increasing the material hardness (Zhong *et al.*, 2018) despite the high fraction of residual porosity.

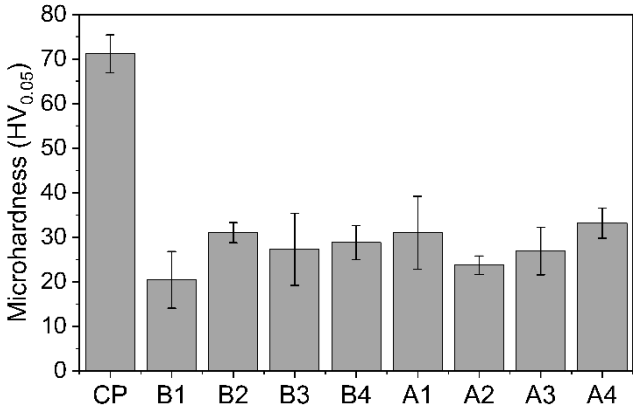

Fig. 19 – Microhardness of samples sintered in dilatometry experiments and in the muffle furnace.

4. Conclusions

In this study, the sintering behaviour of a fine copper powder with average particle size of 3.4 μm processed via cold pressing and via binder jetting additive manufacturing was investigated. The powder material used in the study is the smallest powder reported in the literature regarding powder-based additive manufacturing processes and was selected because previous results showed that the use of fine powders can improve the quality of final parts fabricated through binder jetting. Dilatometry experiments were performed to determine the thermal events that occur during sintering of pure copper powder and the corresponding onset temperatures. Particular attention was paid to the effects of the polymeric binder in binder jetted parts and to powder compaction and plastic deformation effects during sintering of cold-pressed parts. Finally, sintering experiments were performed on binder jetted samples printed with a standard commercial water-based binder, varying the sintering atmosphere, heating rate, peak temperature, and isothermal holding time to explore the effects of processing parameters on the characteristics of final parts. The following conclusions can be drawn based on the experimental results of this work.

- An as-pressed density of 91% was obtained in cold-pressed parts applying a compaction pressure of 333 MPa. Such a high green density has never been reported in the literature for a relatively low compaction pressure. It was attributed to the high fraction of very fine particles, smaller than 2 μm in diameter, which were able to fill the gaps between larger ones, resulting in high density by tight particle packing.
- The onset of sintering in cold-pressed copper parts occurred at around 680 °C and the beginning of a sintering plateau was observed just above 800 °C. These temperature values are lower than those reported by other studies for powder compacts with comparable green density. This was again attributed to the small size of the powder used, resulting in high sintering driving force due to the larger particle free surface area.
- In contrast to previous results, high-density copper powder compacts did not experience swelling and de-densification during the sintering treatment applied in dilatometry experiments. Undesired swelling was avoided by employing a pure copper powder with no antioxidants/lubricants, which prevented the generation of gaseous products due to decomposition of organic compounds at high temperature. Considerable sintering densification took place by applying a relatively moderate energy-intensive treatment, due to the strain energy introduced in cold-pressed parts by powder compression, which reduced the sintering activation energy. A final relative density of about 95.6% was achieved, which resulted in a high microhardness of about 71.2 $HV_{0.05}$.
- Green binder jetted parts used in dilatometry experiments and sintered in the industrial furnace did not undergo an appreciable densification, even considering that they were subjected to a thermal cycle similar to that applied to cold-pressed parts. The lack of sintering was attributed to the insufficient energy provided during the sintering treatment, as loosely packed particles in binder jetted parts have lower inherent sinterability than the compacted and plastically deformed particles in cold-pressed parts. In addition, binder residues and soot contamination produced by incomplete binder combustion hindered neck formation between copper particles. Brown parts showed better sintering, as the binder was more effectively removed during the separate debinding stage.
- Sintering onset occurs at around 900 °C in binder jetted parts, that is significantly higher compared to cold-pressed parts. This confirms that the sintering activation energy of a system made of simply

loosely packed particles is higher than in powder compacts, as the only driving force for sintering is the reduction of particle free surface energy. Brown samples sintered in vacuum exhibited a slightly lower sintering onset temperature and a more uniform densification as compared to parts sintered in argon, because the negative pressure promotes pore closure by extraction of gases, while argon pressure stabilizes residual porosity and promotes pore coalescence.

- The opportunity of sintering in argon/air in the presence of graphite for copper oxide reduction purpose was investigated as an alternative to more complex and expensive procedures with hydrogen-based environments. About 6.9% residual porosity was obtained with air sintering, due to the more efficient formation of reducing CO in a more oxygen-rich atmosphere. However, a much lower microhardness (around 33.2 $HV_{0.05}$) was observed as compared to sample produced by powder metallurgy, as a fine microstructure could not be generated by recrystallization during sintering in the absence of plastic deformation of the copper powder particles. In addition, a relatively high level of carbon residues generated by binder burn-off was found inside residual pores. These impurities are a major defect in copper parts to be used in electronics and thermal management applications because they drastically alter the original thermal and electrical properties of the parent material.

References

Bai, Y., Wagner, G. and Williams, C.B. (2017), "Effect of particle size distribution on powder packing and sintering in binder jetting additive manufacturing of metals", *Journal of Manufacturing Science and Engineering, Transactions of the ASME*, Vol. 139 No. 8, available at:https://doi.org/10.1115/1.4036640.

Bai, Y. and Williams, C.B. (2015), "An exploration of binder jetting of copper", *Rapid Prototyping Journal*, Vol. 21 No. 2, available at:https://doi.org/10.1108/RPJ-12-2014-0180.

Bai, Y. and Williams, C.B. (2018a), "Binder jetting additive manufacturing with a particle-free metal ink as a binder precursor", *Materials and Design*, Vol. 147, available at:https://doi.org/10.1016/j.matdes.2018.03.027.

Bai, Y. and Williams, C.B. (2018b), "The effect of inkjetted nanoparticles on metal part properties in binder jetting additive manufacturing", *Nanotechnology*, Vol. 29 No. 39, available at:https://doi.org/10.1088/1361-6528/aad0bb.

Balluffi, R.W., Allen, S.M. and Carter, W.C. (2005), *Kinetics of Materials: Balluffi/Kinetics*, *Wiley Interscience*.

Bernard, J., Belnou, F., Houivet, D. and Haussonne, J.M. (2005), "Low sintering temperature of MgTiO3 for type I capacitors", *Journal of the European Ceramic Society*, Vol. 25 No. 12 SPEC. ISS., available at:https://doi.org/10.1016/j.jeurceramsoc.2005.03.139.

Blais, C. (2010), "Atmosphere sintering", *Sintering of Advanced Materials*, pp. 165–188.

Castrejón-Sánchez, V.H., Solis, A.C., López, R., Encarnación-Gomez, C., Morales, F.M., Vargas, O.S., Mastache-Mastache, J.E., *et al.* (2019), "Thermal oxidation of copper over a broad temperature range: Towards the formation of cupric oxide (CuO)", *Materials Research Express*, Vol. 6 No. 7, available at:https://doi.org/10.1088/2053-1591/ab1662.

Champion, Y., Bernard, F., Guigue-Millot, N. and Perriat, P. (2003), "Sintering of copper nanopowders under hydrogen: An in situ X-ray diffraction analysis", *Materials Science and Engineering A*, Vol. 360 No. 1–2, available at:https://doi.org/10.1016/S0921-5093(03)00446-5.

Chen, P., Cai, H., Li, Z., Li, M., Wu, H., Su, J., Wen, S., *et al.* (2020), "Crystallization kinetics of polyetheretherketone during high temperature-selective laser sintering", *Additive Manufacturing*, Elsevier B.V., Vol. 36 No. September, p. 101615.

Choudhary, S., Sarma, J.V.N., Pande, S., Ababou-Girard, S., Turban, P., Lepine, B. and Gangopadhyay, S. (2018), "Oxidation mechanism of thin Cu films: A gateway towards the formation of single oxide phase", *AIP Advances*, Vol. 8 No. 5, available at:https://doi.org/10.1063/1.5028407.

Colopi, M., Caprio, L., Demir, A.G. and Previtali, B. (2018a), "Selective laser melting of pure Cu with a 1 kW single mode fiber laser", *Procedia CIRP*, Vol. 74, available at:https://doi.org/10.1016/j.procir.2018.08.030.

Colopi, M., Caprio, L., Demir, A.G. and Previtali, B. (2018b), "Selective laser melting of pure Cu with a 1 kW single mode fiber laser", *Procedia CIRP*, Elsevier B.V., Vol. 74, pp. 59–63.

Dominguez, O., Champion, Y. and Bigot, J. (1998), "Liquidlike Sintering Behavior of Nanometric Fe and Cu

Powders: Experimental Approach", *Metallurgical and Materials Transactions A: Physical Metallurgy and Materials Science*, Vol. 29 No. 12, available at:https://doi.org/10.1007/s11661-998-0201-3.

El-Wardany, T.I., She, Y., Jagdale, V.N., Garofano, J.K., Liou, J.J. and Schmidt, W.R. (2018), "Challenges in Three-Dimensional Printing of High-Conductivity Copper", *Journal of Electronic Packaging, Transactions of the ASME*, Vol. 140 No. 2, available at:https://doi.org/10.1115/1.4039974.

Eriksen, T.E., Ndalamba, P. and Grenthe, I. (1989), "On the corrosion of copper in pure water", *Corrosion Science*, Vol. 29 No. 10, available at:https://doi.org/10.1016/0010-938X(89)90071-1.

Gruber, S., Stepien, L., López, E., Brueckner, F. and Leyens, C. (2021), "Physical and geometrical properties of additively manufactured pure copper samples using a green laser source", *Materials*, available at:https://doi.org/10.3390/ma14133642.

Guschlbauer, R., Burkhardt, A.K., Fu, Z. and Körner, C. (2020), "Effect of the oxygen content of pure copper powder on selective electron beam melting", *Materials Science and Engineering A*, Vol. 779 No. July 2019, available at:https://doi.org/10.1016/j.msea.2020.139106.

Hammad, F.H. (1990), "Application of the Hall-Petch Relation to Microhardness", Vol. 455.

Ikeshoji, T.T., Nakamura, K., Yonehara, M., Imai, K. and Kyogoku, H. (2018), "Selective Laser Melting of Pure Copper", *Jom*, Springer US, Vol. 70 No. 3, pp. 396–400.

Jadhav, S.D., Dadbakhsh, S., Goossens, L., Kruth, J.P., Van Humbeeck, J. and Vanmeensel, K. (2019), "Influence of selective laser melting process parameters on texture evolution in pure copper", *Journal of Materials Processing Technology*, Vol. 270, available at:https://doi.org/10.1016/j.jmatprotec.2019.02.022.

Jadhav, S.D., Goossens, L.R., Kinds, Y., Hooreweder, B. Van and Vanmeensel, K. (2021), "Laser-based powder bed fusion additive manufacturing of pure copper", *Additive Manufacturing*, Vol. 42, available at:https://doi.org/10.1016/j.addma.2021.101990.

Jiang, Q., Zhang, P., Yu, Z., Shi, H., Wu, D., Yan, H., Ye, X., *et al.* (2021), "A review on additive manufacturing of pure copper", *Coatings*, Vol. 11 No. 6, available at:https://doi.org/10.3390/coatings11060740.

Johnston, S., Frame, D., Anderson, R. and Storti, D. (2004), "Strain Analysis of Initial Stage Sintering of 316L SS Three Dimensionally Printed (3DP ™) Components 1 Introduction 2 Background on Current Initial Stage Sintering", *Current*, Vol. di.

Jones, H.A. and Taylor, H.S. (1923), "The Reduction of Copper Oxide by Carbon Monoxide and the Catalytic Oxidation of Carbon Monoxide in the Presence of Copper and Copper Oxide", *The Journal of Physical Chemistry*, Vol. 27 No. 7, available at:https://doi.org/10.1021/j150232a002.

Juan, H.-L. (2017), "Effect of temperature ratio (Ts/Tm) and time on the sintering behavior of metallic 316L stainless steel coupons produced using jet-binder technology".

Khasanshin, T.S. and Aleksandrov, A.A. (1984), "Thermodynamic properties of ethanol at atmospheric pressure", *Journal of Engineering Physics*, Vol. 47 No. 3, available at:https://doi.org/10.1007/BF00873717.

Kumar, A., Bai, Y., Eklund, A. and Williams, C.B. (2017), "Effects of Hot Isostatic Pressing on Copper Parts Fabricated via Binder Jetting", *Procedia Manufacturing*, Vol. 10, available at:https://doi.org/10.1016/j.promfg.2017.07.084.

Ledford, C., Rock, C., Carriere, P., Frigola, P., Gamzina, D. and Horn, T. (2019), "Characteristics and processing of hydrogen-treated copper powders for EB-PBF additive manufacturing", *Applied Sciences (Switzerland)*, Vol. 9 No. 19, available at:https://doi.org/10.3390/app9193993.

Ledford, C., Rock, C., Tung, M., Wang, H., Schroth, J. and Horn, T. (2020), "Evaluation of electron beam powder bed fusion additive manufacturing of high purity copper for overhang structures using in-situ real time backscatter electron monitoring", Vol. 48, available at:https://doi.org/10.1016/j.promfg.2020.05.120.

Li, J., Vizkelethy, G., Revesz, P., Mayer, J.W., Matienzo, L.J., Emmi, F., Ortega, C., *et al.* (1991), "Influence of carbon on the enhanced oxygen loss in copper oxide films", *Applied Physics Letters*, Vol. 58 No. 12, available at:https://doi.org/10.1063/1.104305.

Li, M., Du, W., Elwany, A., Pei, Z. and Ma, C. (2020), "Metal binder jetting additive manufacturing: A literature review", *Journal of Manufacturing Science and Engineering, Transactions of the ASME*,

available at:https://doi.org/10.1115/1.4047430.

Liu, L., Zhang, T.J., Cui, K. and Dong, Y.D. (1999), "Reduction of copper oxide with graphite by mechanical alloying", *Journal of Materials Research*, Vol. 14 No. 10, available at:https://doi.org/10.1557/JMR.1999.0548.

Lodes, M.A., Guschlbauer, R. and Körner, C. (2015), "Process development for the manufacturing of 99.94% pure copper via selective electron beam melting", *Materials Letters*, Elsevier, Vol. 143, pp. 298–301.

Lykov, P., Baytimerov, R., Vaulin, S., Safonov, E. and Zherebtsov, D. (2016), "Selective Laser Melting of Copper by 200 W CO2 Laser", *SAE Technical Papers*, pp. 2016–2019.

Lykov, P.A., Safonov, E. V. and Akhmedianov, A.M. (2016), "Selective laser melting of copper", *Materials Science Forum*, Vol. 843 No. February, pp. 284–288.

Mahmoud, M.M., Link, G. and Thumm, M. (2015), "The role of the native oxide shell on the microwave sintering of copper metal powder compacts", *Journal of Alloys and Compounds*, Vol. 627, available at:https://doi.org/10.1016/j.jallcom.2014.11.180.

Mariani, M., Beltrami, R., Brusa, P., Galassi, C., Ardito, R. and Lecis, N. (2021), "3D printing of fine alumina powders by binder jetting", *Journal of the European Ceramic Society*, Vol. 41 No. 10, available at:https://doi.org/10.1016/j.jeurceramsoc.2021.04.006.

Masuda, Y. (1962), "235856528.pdf".

Miyanaji, H., Rahman, K.M., Da, M. and Williams, C.B. (2020), "Effect of fine powder particles on quality of binder jetting parts", *Additive Manufacturing*, Vol. 36, available at:https://doi.org/10.1016/j.addma.2020.101587.

Olmos, L., Bouvard, D., Salvo, L., Bellet, D. and Di Michiel, M. (2014), "Characterization of the swelling during sintering of uniaxially pressed copper powders by in situ X-ray microtomography", *Journal of Materials Science*, Vol. 49 No. 12, available at:https://doi.org/10.1007/s10853-014-8117-3.

Onuike, B., Heer, B. and Bandyopadhyay, A. (2018), "Additive manufacturing of Inconel 718—Copper alloy bimetallic structure using laser engineered net shaping (LENS™)", *Additive Manufacturing*, Vol. 21, available at:https://doi.org/10.1016/j.addma.2018.02.007.

Papillon, A., Missiaen, J.M., Chaix, J.M., Roure, S. and Schellekens, H. (2017), "Sintering mechanisms of Cu-Cr metallic composites", *International Journal of Refractory Metals and Hard Materials*, Vol. 65, available at:https://doi.org/10.1016/j.ijrmhm.2016.11.010.

Papillon, A., Roure, S., Schellekens, H., Missiaen, J.M., Chaix, J.M. and Rigal, E. (2017), "Investigation on the chemical reactions affecting the sinterability and oxide content of Cu–Cr composites during the solid state sintering process", *Materials and Design*, Vol. 113, available at:https://doi.org/10.1016/j.matdes.2016.09.038.

Raship, N.A., Sahdan, M.Z., Adriyanto, F., Nurfazliana, M.F. and Bakri, A.S. (2017), "Effect of annealing temperature on the properties of copper oxide films prepared by dip coating technique", *AIP Conference Proceedings*, Vol. 1788, available at:https://doi.org/10.1063/1.4968374.

Sabzevari, M., Sajjadi, S.A. and Moloodi, A. (2016), "Physical and mechanical properties of porous copper nanocomposite produced by powder metallurgy", *Advanced Powder Technology*, Vol. 27 No. 1, available at:https://doi.org/10.1016/j.apt.2015.11.005.

Silbernagel, C., Gargalis, L., Ashcroft, I., Hague, R., Galea, M. and Dickens, P. (2019), "Electrical resistivity of pure copper processed by medium-powered laser powder bed fusion additive manufacturing for use in electromagnetic applications", *Additive Manufacturing*, Elsevier, Vol. 29 No. November 2018, p. 100831.

Tran, T.Q., Chinnappan, A., Lee, J.K.Y., Loc, N.H., Tran, L.T., Wang, G., Kumar, V.V., *et al.* (2019), "3D printing of highly pure copper", *Metals*, available at:https://doi.org/10.3390/met9070756.

Trevisan, F., Calignano, F., Lorusso, M., Lombardi, M., Manfredi, D. and Fino, P. (2017), "Selective laser melting of chemical pure copper powders", *Proceedings Euro PM 2017: International Powder Metallurgy Congress and Exhibition*, No. October.

Wheat, E., Shanbhag, G. and Vlasea, M. (2020), "The master sinter curve and its application to binder jetting additive manufacturing", *Journal of Manufacturing Science and Engineering, Transactions of the ASME*, Vol. 142 No. 10, available at:https://doi.org/10.1115/1.4047140.

Yegyan Kumar, A., Bai, Y., Eklund, A. and Williams, C.B. (2018), "The effects of Hot Isostatic Pressing on

parts fabricated by binder jetting additive manufacturing", *Additive Manufacturing*, Vol. 24, available at:https://doi.org/10.1016/j.addma.2018.09.021.

Yegyan Kumar, A., Wang, J., Bai, Y., Huxtable, S.T. and Williams, C.B. (2019), "Impacts of process-induced porosity on material properties of copper made by binder jetting additive manufacturing", *Materials and Design*, Vol. 182, available at:https://doi.org/10.1016/j.matdes.2019.108001.

Zhong, H.Z., Li, C.G., Zhang, X.Y. and Gu, J.F. (2018), "The graded microstructures evolving with thermal cycles in pure copper processed by laser metal deposition", Vol. 230, pp. 215–218.